Simultaneous multiscale measurements on dynamic deformation of a magnesium alloy with synchrotron x-ray imaging and diffraction

L. Lu[a,b,c], T. Sun[d], K. Fezzaa[d], X.L. Gong[a,*], S.N. Luo[b,c,**]

[a] *CAS Key Laboratory of Mechanical Behavior and Design of Materials, Department of Modern Mechanics, University of Science and Technology of China, Hefei, Anhui 230027, PR China*
[b] *Key Laboratory of Advanced Technologies of Materials, Ministry of Education, Southwest Jiaotong University, Chengdu, Sichuan 610031, PR China*
[c] *The Peac Institute of Multiscale Sciences, Chengdu, Sichuan 610031, PR China*
[d] *Advanced Photon Source, Argonne National Laboratory, Argonne, IL 60439, USA*

ARTICLE INFO

ABSTRACT

Dynamic split Hopkinson pressure bar experiments with *in situ* synchrotron x-ray imaging and diffraction are conducted on a rolled magnesium alloy at high strain rates of ~5500 s^{-1}. High speed multiscale measurements including stress–strain curves (macroscale), strain fields (mesoscale), and diffraction patterns (microscale) are obtained simultaneously, revealing strong anisotropy in deformation across different length scales. {10$\bar{1}$2} extension twinning induces homogenized strain fields and gives rise to rapid increase in strain hardening rate, while dislocation motion leads to inhomogeneous deformation and a decrease in strain hardening rate. During the early stage of plastic deformation, twinning is dominant in dynamic compression, while dislocation motion prevails in quasi-static loading, manifesting a strain-rate dependence of deformation.

1. Introduction

Measurements on deformation across multiple temporal and spatial scales are critical to making concrete connections between different scales indispensable for the development of physics-based models. In order to make such connections, it is important to capture *in situ*, in real time, deformation simultaneously at different length scales, particularly at meso- and microscales. Recently, multiscale measurements have been employed to investigate fibrin clot extension [1] and plasma flows [2]. It is highly desirable to extend multiscale measurements into metal deformation at high strain rates, which is essentially unexplored.

Magnesium has a hexagonal close-packed structure. Its deformation modes include (0001)⟨a⟩ basal slip [3], {10$\bar{1}$0}⟨a⟩ prismatic slip, {10$\bar{1}$1}⟨a⟩ and {11$\bar{2}$2}⟨c + a⟩ pyramidal slip [4,5], {10$\bar{1}$2} extension twin, {10$\bar{1}$1} contraction twin, and {10$\bar{1}$1} − {10$\bar{1}$2} double twin [6–12]. Strong anisotropy in deformation is characteristic of magnesium and its alloys under quasi-static compression, and associated with such deformation modes [13–15]. The stress and strain hardening rate curves for different loading directions exhibit drastic differences. For compression perpendicular to the *c*-axis in textured samples, three distinct regimes (I–III) are observed [15–20]. Multiscale measurements revealed that extension twinning (microscale) induces homogenized strain fields (mesoscale), which in turn lead to increase in strain hardening rate

(macroscale) [15]. Deformation of magnesium alloys under high strain rate compression shows similar anisotropy [21–23]. Dixit et al. [23] argued that the high degree of strain hardening is due to texture hardening associated with extension twinning, coupled with significant increase in dislocation density with increasing strain, on the basis of stress–strain curves and *ex situ* analysis of twinning and dislocation motion. However, simultaneous, *in situ*, real-time, multiscale, measurements on their dynamic deformation are still lacking.

In this work, we use magnesium alloy AZ31 as an example to demonstrate simultaneous, high-speed, multiscale measurements under high strain rate compression. Multiscale measurements on macroscale stress–strain curves, mesoscale strain fields, and microstructure evolution are obtained simultaneously with synchrotron x-ray digital image correlation (XDIC) and x-ray diffraction. Electron back-scatter diffraction (EBSD) is conducted to characterize deformation twins in recovered specimens. Such measurements reveal anisotropy in its deformation across different spatial scales, and allow us to make connections between them. Extension twinning induces homogenized strain fields and gives rise to rapid increase in strain hardening rate, while it is the opposite for dislocation motion. Comparison with quasi-static loading shows a strain-rate dependence of deformation in this alloy.
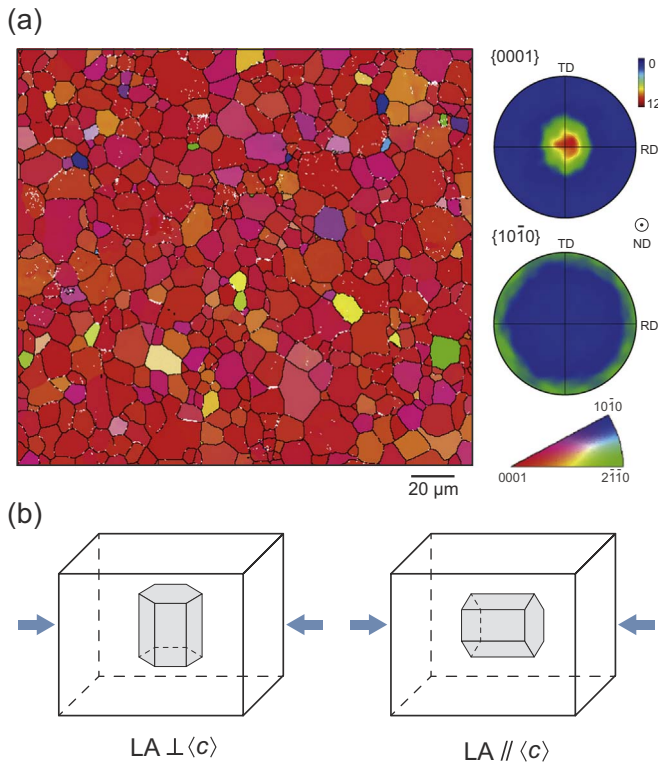

(a)

(b)

Fig. 1. (a) Inverse pole figure map and pole figures of rolled magnesium alloy AZ31, viewed along the normal direction (ND). (b) Illustrations of the relative orientation of the loading axis (LA) with respect to the *c*-axis.

2. Materials and experiments

A commercial rolled AZ31 magnesium alloy is used for dynamic compression tests. Fig. 1(a) shows inverse pole figure and pole figures obtained with EBSD. The average grain size is ~10 μm. The crystallographic *c*-axis, ⟨*c*⟩, in most grains is closely aligned with the normal direction (ND, Fig. 1(a)). We thus refer to ND as ⟨*c*⟩ in the following discussions. For EBSD analysis, the samples are mechanically ground and polished with 2 μm and 0.5 μm diamond particles, and then electro-etched in a solution composed of 10% perchloric acid and 90% ethanol at 5 volts, with a copper rod and the sample as electrodes. EBSD characterization is performed in a field emission gun SEM (FEI Quanta 250) equipped with an Oxford EBSD detector. EBSD scan is performed with a 25 kV accelerating voltage at a working distance of 15 mm, using a 0.5 μm step size.

Cuboidal specimens as illustrated in Fig. 1(b) are prepared via electrical discharge machining; their dimensions perpendicular to the x-ray beam direction are 2.6×2.0 mm^2, and the thickness along the beam direction is 1.0 mm. Two kinds of compression tests are conducted, for which the loading axis (LA) is either perpendicular or parallel to ⟨*c*⟩; they are referred to as LA⊥⟨*c*⟩ and LA∥⟨*c*⟩, respectively (Fig. 1(b)). For XDIC, the specimens are etched with perchloric acid to produce x-ray speckles [24].

High strain rate compression tests are performed at room temperature using a miniature split Hopkinson pressure bar (SHPB) at beamline 32-ID-B of the Advanced Photon Source. The experimental setup is shown in Fig. 2 for simultaneous, multiframe, transient x-ray diffraction [25,26] and phase contrast imaging [24,27] measurements under dynamic compression. Both incident (1) and transmission (4) bars with a diameter of 6 mm are made of high-strength steel. When a striker impacts the incident bar, a compressional elastic wave is created, propagating along the *x*-direction (Fig. 2). When the incident wave arrives at the interface between the incident bar and the sample (3), it is partially reflected owing to impedance mismatch, while the
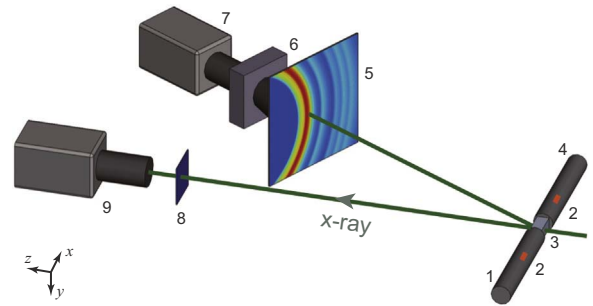

Fig. 2. Schematic of the experimental setup for simultaneous x-ray diffraction and imaging under high strain rate compression, along with the coordinate system (*xyz*). 1: incident bar; 2: strain gages; 3: sample; 4: transmission bar; 5: diffraction scintillator (with illustrative diffraction rings of the magnesium alloy); 6: microchannel plate; 7: diffraction camera; 8: imaging scintillator; 9: imaging camera.

rest is transmitted into the transmission bar. The incident, reflected and transmitted waves are recorded by strain gages (2). Upon loading, the x-rays transmitted through the sample impinge on an imaging scintillator (8), and the scattered x-rays, on a diffraction scintillator (5). A microchannel plate (6) is used to intensify the optical signals converted from the scattered x-rays, and synchronized with the diffraction camera (7). The recording cameras for both imaging (9) and diffraction (7) are Photron Fastcam SA-Z. The exposure times for imaging and diffraction are 347 ns and 1 μs, respectively, while their frame intervals are the same (10 μs). The HiSPoD program [28] is utilized to index the diffraction rings and convert them into one-dimensional diffraction pattern (intensity versus 2θ) by azimuthal integration. Similar experimental details were presented elsewhere [26,29,30].

The stress (σ), strain (ε), and strain rate ($\dot{\varepsilon}$) histories of a sample can be calculated with the strain gage signals according to the following equations

$$\sigma(t) = -\frac{A_t}{A_s} E_t \varepsilon_t(t), \tag{1}$$

$$\varepsilon(t) = -\frac{2C_0}{L_s} \int_0^t [\varepsilon_t(\tau) - \varepsilon_i(\tau)] d\tau, \tag{2}$$

$$\dot{\varepsilon}(t) = -\frac{2C_0}{L_s}(\varepsilon_t(t) - \varepsilon_i(t)), \tag{3}$$

where E is the Young's modulus, A is the cross-sectional area, and t and τ denote time. C_0 is the elastic velocity of the bar. L_s is the length of the sample. Subscripts s, i and t denote sample, incident and transmission bar, respectively.

3. Experimental results

3.1. Macroscale mechanical behavior

The true stress–strain ($\sigma - \varepsilon$) curves and corresponding strain hardening rate curves for two loading directions, LA⊥⟨*c*⟩ and LA∥⟨*c*⟩, under a strain rate of ~5500 s^{-1}, are shown in Fig. 3. The yield stresses along both compression directions are similar (~110 MPa). The $\sigma - \varepsilon$ curve for the LA⊥⟨*c*⟩ loading exhibits a sigmoidal shape, while that for the LA∥⟨*c*⟩ loading is concave downward. The strain hardening rate for the LA∥⟨*c*⟩ loading decreases monotonically. In contrast, the strain hardening rate versus true strain (dσ/dε–ε) curve for the LA⊥⟨*c*⟩ loading demonstrates three regimes: the strain hardening rate decreases rapidly upon initial yield, as expected for an elastic–plastic transition (regime I); the rate then experiences a distinct increase followed by a sharp decrease (regimes II and III, respectively).

3.2. Mesoscale strain fields

During dynamic compression, image sequences are acquired via
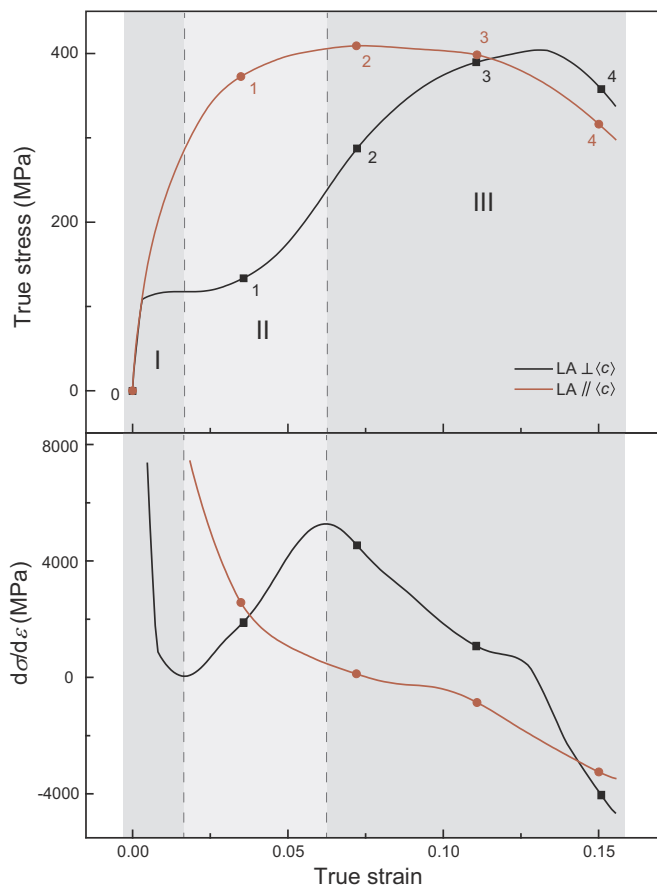
Fig. 3. Stress–strain curves and the corresponding strain hardening rate curves for two different loading directions, LA⊥⟨c⟩ and LA∥⟨c⟩. The symbols (10 µs apart) denote the instants for simultaneous imaging and diffraction measurements. The curves are divided into three regimes, I–III. Numbers 0–4 represent instants t_0–t_4.

synchrotron x-ray phase contrast imaging [27]. To understand mesoscale deformation and damage mechanisms, the image sequences are used to map the strain fields with XDIC [24]. The XDIC method resorts to uniformly distributed x-ray speckles which are originated from surface roughness or internal isolated structure features, and "traces" the speckles in x-ray images to resolve displacements via image correlation between two adjacent frames. The Green-Lagrange normal strains (E_{xx}) is calculated from displacement (u) gradients as

$$E_{ij} = \frac{1}{2}(u_{i,j} + u_{j,i} + u_{k,i}u_{k,j}), \tag{4}$$

where $i, j, k = x, y$. The normal strain fields, $E_{xx}(x, y)$, for the LA∥⟨c⟩ and LA⊥⟨c⟩ loading obtained at instants noted in Fig. 3, are shown in Fig. 4. The areas with poor correlation are replaced with white pixels.

The dynamic mesoscale deformation maps in Fig. 4 show that the LA∥⟨c⟩ sample experiences continuous local deformation accumulation (t_1–t_3) after the elastic–plastic transition (t_0–t_1). Unlike the LA∥⟨c⟩ case, the normal strain field maps (E_{xx}) for the LA⊥⟨c⟩ loading show relatively homogeneous deformation (t_1), and then a slight accumulation of localized plastic strain (t_2–t_3). Eventually, both LA∥⟨c⟩ and LA⊥⟨c⟩ samples undergo shear fracture (Fig. 4), consistent with strain concentration features (t_3).

3.3. Microscale deformation

In addition to phase contrast imaging, simultaneous x-ray diffraction measurement is performed. Diffraction patterns (intensity versus 2θ) at corresponding instants (t_0–t_4) are shown in Fig. 5 for two different loading directions: LA∥⟨c⟩ and LA⊥⟨c⟩. Schematics of grain

orientations contributing to {0002} and {10̄10} diffraction peaks are shown in Fig. 5 insets. As a result of the initial texture, the {0002} basal plane reflection dominates the {10̄10} prismatic plane reflection for the undeformed LA∥⟨c⟩ sample, and it is the opposite for the undeformed LA⊥⟨c⟩ sample (Fig. 5).

Previous studies demonstrated that the {0002} peak intensity is augmented by extension twinning but reduced by dislocation motion [15]. As plastic deformation proceeds, the {0002} peak intensity of the LA∥⟨c⟩ sample decreases continuously (t_0–t_4). It can be inferred that few twins are activated, and the plastic deformation is mainly achieved by dislocation motion. Nevertheless, the {0002} reflection for the LA⊥⟨c⟩ sample undergoes a pronounced growth and eventually dominates all the other diffraction peaks (t_0–t_3) with increasing strain, indicating that numerous grains alter their c-axis orientations to become parallel to LA by {10̄12} extension twinning (~ 90° re-orientation) [15,31]. Then, the {0002} reflection gradually declines, and dislocation motion dominates twinning during t_2–t_4.

As a complement to *in situ* measurements, *ex situ* EBSD is utilized to analyze the cross-sections of postmortem samples. Image quality maps of the LA⊥⟨c⟩ and LA∥⟨c⟩ samples deformed at a true strain of 0.06 are shown in Fig. 6, and three primary types of deformation twins formed during dynamic compression are depicted with different colors. For the LA⊥⟨c⟩ loading, massive {10̄12} extension twins and a few {10̄11} contraction twins and {10̄11} − {10̄12} double twins are activated. However, for the LA∥⟨c⟩ sample, the number of {10̄12} extension twins is reduced, but more pronounced activation of {10̄11} − {10̄12} double twins is observed. Since the secondary {10̄12} twins develop within the {10̄11} contraction twins, it is expected that the {10̄11} contraction twins are activated prior to double twins, although few {10̄11} contraction twins survive (Fig. 7).

4. Discussions

Multiscale measurements are obtained under high strain rate loading ($10^3 - 10^4\,\mathrm{s}^{-1}$) in terms of true stress–strain ($\sigma - \varepsilon$) curves (macroscale), strain fields (mesoscale) and diffraction patterns (microscale). The strain fields for the LA∥⟨c⟩ loading exhibit significant localization. Previous studies reported that the {10̄11} − {10̄12} double twinning can lead to localization and failure in single crystals by rotating the basal plane into an orientation favorable to glide [31]. In addition, only a small number of {10̄11} − {10̄12} twins are activated in our experiments. As a result, dislocation motion prevails over twinning during plastic deformation and leads to strain localization. Dislocations nucleated at such defects as grain boundaries induce strain concentrations. The localization is attributed to short slide length and pileup of dislocations. Consequently, its macroscale stress-strain curve exhibits a decrease in strain hardening rate due to mesoscale inhomogeneous deformation in regimes II and III.

On the other hand, for the LA⊥⟨c⟩ loading, abundant {10̄12} extension twins are activated in regime II and result in homogenization of plastic deformation as manifested in strain fields, giving rise to the pronounced increase in strain hardening rate. Twin boundaries are planar and efficiently sweep across a larger sample area. Thus, the stress gradients can be reduced by twinning to achieve homogeneous deformation within a short period of time, and the reduction in strain localization effectively boosts strain hardening rate. As dislocation motion dominates twinning, strain hardening rate begins to decline in regime III.

Dynamic compression of magnesium alloy AZ31 shows a strong anisotropy under different loading directions, and similar anisotropy has been observed under quasi-static compression [15]. In order to investigate the influence of strain rate on strain field evolution, the degrees of inhomogeneity of normal strain fields as a function of true strain under dynamic and quasi-static compression [15] are calculated (Fig. 6). The degree of inhomogeneity ($\mathscr{C}$) is quantified by the coefficient of spatial variation of E_{xx}, defined as
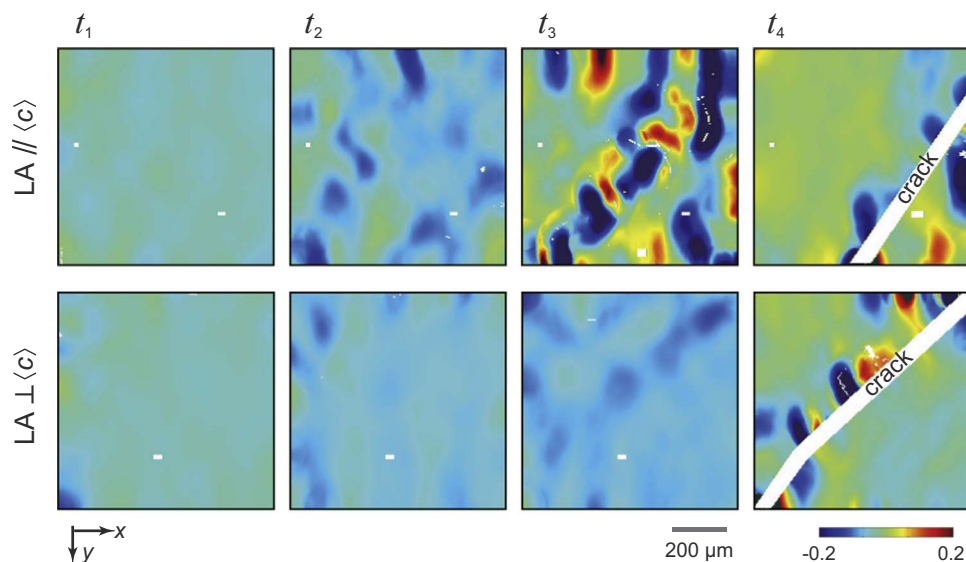
Fig. 4. Green-Lagrange normal strain field maps (E_{xx}) at instants t_1–t_4 obtained from XDIC for two different loading directions, LA$\|\langle c\rangle$ and LA$\perp\langle c\rangle$.
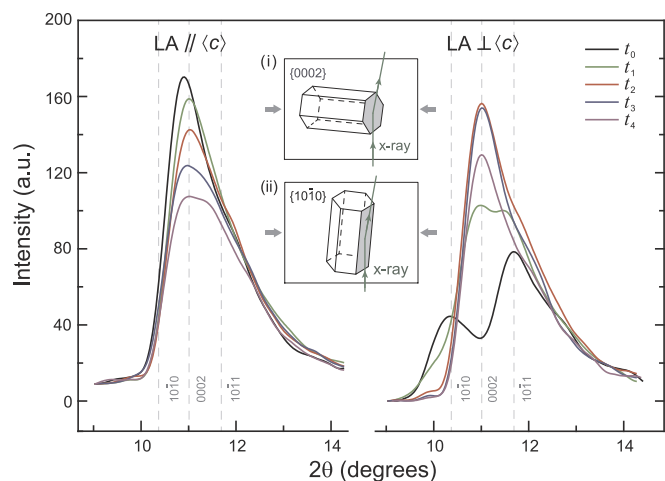

Fig. 5. X-ray diffraction peak intensities at instants t_0–t_4 for the two loading directions. Insets: grain orientations contributing to diffraction peaks {0002} and {10$\bar{1}$0}.

$$\mathscr{C} = \frac{\text{Stdev}(E_{xx})}{\text{Avg}(E_{xx})}, \tag{5}$$

where Stdev and Avg are the standard deviation and average of normal strain field, respectively.

During the initial stage of plastic deformation ($\varepsilon < 0.05$), the $\mathscr{C}_d$ values (subscript d denotes dynamic; solid lines in Fig. 6) are much smaller than the $\mathscr{C}_s$ values (quasi-static, dash lines in Fig. 6). For small plastic deformation, more twins are activated to achieve more homogeneous deformation under dynamic compression, while dislocation motion prevails under quasi-static compression, regardless of loading directions. This is consistent with the observation that increased strain rates lead to increasing deformation twinning [32–34]. Furthermore, elevated temperature can lead to more homogeneous deformation [35]; thermally activated mechanisms by localized heating under dynamic compression induce more homogenized strain field as well. Initially, increasing strain and twinning induce a certain decrease in $\mathscr{C}_s$; dislocation motion then becomes dominant, so $\mathscr{C}_d$ and $\mathscr{C}_s$ increase rapidly. In addition, since extension twins can be readily activated when the compression axis is perpendicular to the crystallographic c-axes [12], the $\mathscr{C}$ values for the LA$\perp\langle c\rangle$ samples are lower than those for the LA$\|\langle c\rangle$ samples under both dynamic and quasi-static compression. Degrees of
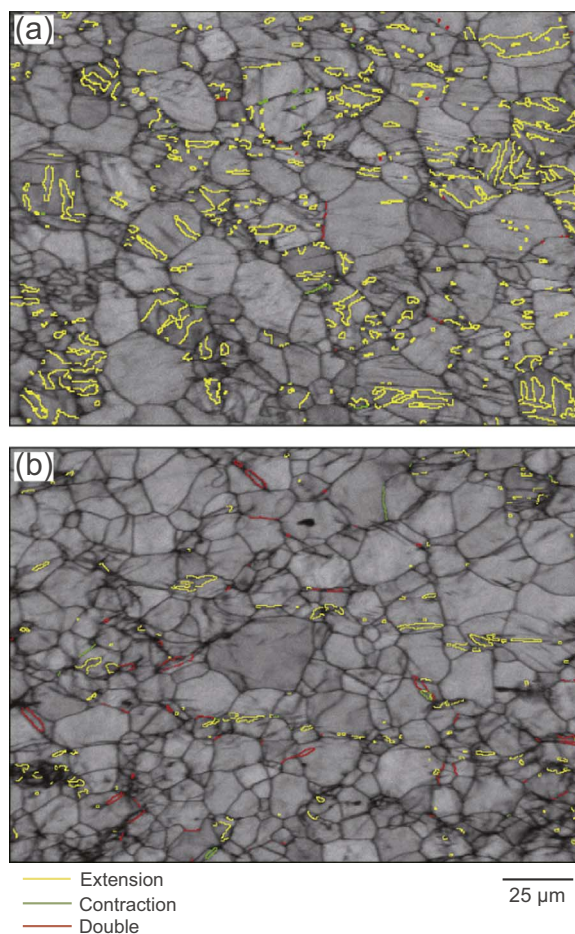

Fig. 6. Image quality maps overlaid with twin boundaries for the LA$\perp\langle c\rangle$ (a) and LA$\|\langle c\rangle$ (b) loading. The samples are collected at a true strain level of 0.06. Yellow curves refer to extension twin boundaries (86.3°$\langle1\bar{2}10\rangle \pm 5$°), green curves to contraction twin boundaries (56.2°$\langle1\bar{2}10\rangle \pm 5$°), and red curves to double twin boundaries (37.5°$\langle1\bar{2}10\rangle \pm 5$°). The loading axis is horizontal. (For interpretation of the references to color in this figure legend, the reader is referred to the web version of this article.).
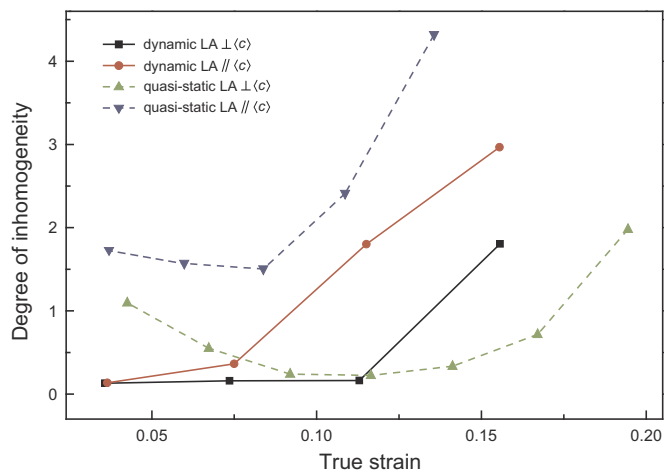
Fig. 7. Degrees of inhomogeneity of normal strain fields as a function of true strain under dynamic (solid curves) and quasi-static (dashed curves), obtained form Ref. [15].

inhomogeneity derived from strain fields are an indicator of deformation mechanisms in magnesium alloys (dislocation motion or twinning), useful for investigating different microstructure evolutions under various strain rates.

5. Conclusions

SHPB experiments are conducted to investigate dynamic response of a rolled magnesium alloy AZ31 along the LA⊥⟨c⟩ or LA∥⟨c⟩ direction under a strain rate of ~ 5500 s^{-1}, in conjunction with *in situ* synchrotron x-ray imaging and diffraction. Multiscale measurements on macroscale stress–strain curves (from strain gages), mesoscale strain fields (XDIC), and microscale deformation (diffraction) are achieved simultaneously. Deformation twins are characterized with EBSD. Such measurements bear potential applications to other materials and processes. The degree of inhomogeneity derived from strain fields can be used to make connections between strain field and dislocation motion or twinning.

The stress–strain curves and corresponding strain hardening rate curves for the LA⊥⟨c⟩ and LA∥⟨c⟩ loading show strong anisotropy in deformation (regimes I–III), and XDIC and diffraction measurements show consistent features. When the {10$\bar{1}$2} extension twinning prevails, strain field is homogenized, and reduced strain localizations effectively boost strain hardening rate. When dislocation motion is dominant, dislocations nucleated at defects induce strain concentrations, and such mesoscale inhomogeneous deformation lowers strain hardening rate. All these characteristics are similar to those for quasi-static compression. However, during the initial stage of plastic deformation, twinning dominates dislocation motion under dynamic compression, while it is the opposite under quasi-static loading. Thus, deformation of magnesium alloy AZ31 also shows strain rate dependence.

Acknowledgments

References

[1] A.E. Brown, R.I. Litvinov, D.E. Discher, P.K. Purohit, J.W. Weisel, Multiscale mechanics of fibrin polymer: gel stretching with protein unfolding and loss of water, Science 325 (2009) 741–744.

[2] S. Leerink, V. Bulanin, A. Gurchenko, E. Gusakov, J. Heikkinen, S. Janhunen, S. Lashkul, A. Altukhov, L. Esipov, M.Y. Kantor, T. Kiviniemi, T. Korpilo, D. Kuprienko, A. Petrov, Multiscale investigations of drift-wave turbulence and plasma flows: measurements and total-distribution-function gyrokinetic simulations, Phys. Rev. Lett. 109 (2012) 165001.

[3] C.S. Roberts, Magnesium and its Alloys, Wiley, New York, 1960.

[4] A. Staroselsky, L. Anand, A constitutive model for hcp materials deforming by slip and twinning: application to magnesium alloy AZ31B, Int. J. Plast. 19 (2003) 1843–1864.

[5] A. Chapuis, J.H. Driver, Temperature dependency of slip and twinning in plane strain compressed magnesium single crystals, Acta Mater. 59 (2011) 1986–1994.

[6] M.R. Barnett, Z. Keshavarz, A.G. Beer, D. Atwell, Influence of grain size on the compressive deformation of wrought Mg-3Al-1Zn, Acta Mater. 52 (2004) 5093–5103.

[7] M.D. Nave, M.R. Barnett, Microstructures and textures of pure magnesium deformed in plane-strain compression, Scr. Mater. 51 (2004) 881–885.

[8] S.H. Park, S.G. Hong, C.S. Lee, Activation mode dependent {10-12} twinning characteristics in a polycrystalline magnesium alloy, Scr. Mater. 62 (2010) 202–205.

[9] N.V. Dudamell, I. Ulacia, F. Gálvez, S. Yi, J. Bohlen, D. Letzig, I. Hurtado, M.T. Pérez-Prado, Twinning and grain subdivision during dynamic deformation of a Mg AZ31 sheet alloy at room temperature, Acta Mater. 59 (2011) 6949–6962.

[10] N. Stanford, M. Barnett, Effect of composition on the texture and deformation behaviour of wrought Mg alloys, Scr. Mater. 58 (2008) 179–182.

[11] I. Basu, T. Al-Samman, Twin recrystallization mechanisms in magnesium-rare earth alloys, Acta Mater. 96 (2015) 111–132.

[12] M. Wang, L. Lu, C. Li, X.H. Xiao, X.M. Zhou, J. Zhu, S.N. Luo, Deformation and spallation of a magnesium alloy under high strain rate loading, Mater. Sci. Eng. A 661 (2016) 126–131.

[13] S.R. Agnew, Ö. Duygulu, Plastic anisotropy and the role of non-basal slip in magnesium alloy AZ31B, Int. J. Plast. 21 (2005) 1161–1193.

[14] J. Bohlen, M.R. Nürnberg, J.W. Senn, D. Letzig, S.R. Agnew, The texture and anisotropy of magnesium-zinc-rare earth alloy sheets, Acta Mater. 55 (2007) 2101–2112.

[15] L. Lu, J.W. Huang, D. Fan, B.X. Bie, T. Sun, K. Fezzaa, X.L. Gong, S.N. Luo, Anisotropic deformation of extruded magnesium alloy AZ31 under uniaxial compression: a study with simultaneous in situ synchrotron x-ray imaging and diffraction, Acta Mater. 120 (2016) 86–94.

[16] M. Lentz, M. Klaus, I.J. Beyerlein, M. Zecevic, W. Reimers, M. Knezevic, In situ X-ray diffraction and crystal plasticity modeling of the deformation behavior of extruded Mg-Li-(Al) alloys: an uncommon tension-compression asymmetry, Acta Mater. 86 (2015) 254–268.

[17] M. Knezevic, A. Levinson, R. Harris, R.K. Mishra, R.D. Doherty, S.R. Kalidindi, Deformation twinning in AZ31: influence on strain hardening and texture evolution, Acta Mater. 58 (2010) 6230–6242.

[18] H. El Kadiri, A.L. Oppedal, A crystal plasticity theory for latent hardening by glide twinning through dislocation transmutation and twin accommodation effects, J. Mech. Phys. Solids 58 (2010) 613–624.

[19] D. Sarker, D.L. Chen, Detwinning and strain hardening of an extruded magnesium alloy during compression, Scr. Mater. 67 (2012) 165–168.

[20] Q. Ma, H. El Kadiri, A.L. Oppedal, J.C. Baird, B. Li, M.F. Horstemeyer, S.C. Vogel, Twinning effects in a rod-textured AM30 Magnesium alloy, Int. J. Plast. 29 (2012) 60–76.

[21] M.T. Tucker, M.F. Horstemeyer, P.M. Gullett, H.E. Kadiri, W.R. Whittington, Anisotropic effects on the strain rate dependence of a wrought magnesium alloy, Scr. Mater. 60 (2009) 182–185.

[22] I. Ulacia, N.V. Dudamell, F. Gálvez, S. Yi, M.T. Pérez-Prado, I. Hurtado, Mechanical behavior and microstructural evolution of a Mg AZ31 sheet at dynamic strain rates, Acta Mater. 58 (2010) 2988–2998.

[23] N. Dixit, K.Y. Xie, K.J. Hemker, K.T. Ramesh, Microstructural evolution of pure magnesium under high strain rate loading, Acta Mater. 87 (2015) 56–67.

[24] L. Lu, D. Fan, B.X. Bie, X.X. Ran, M.L. Qi, N. Parab, J.Z. Sun, H.J. Liao, M.C. Hudspeth, B. Claus, K. Fezzaa, T. Sun, W. Chen, X.L. Gong, S.N. Luo, Note: dynamic strain field mapping with synchrotron X-ray digital image correlation, Rev. Sci. Instrum. 85 (2014) 076101.

[25] P. Lambert, C. Hustedt, K. Vecchio, E. Huskins, D. Casem, S. Gruner, M. Tate, H. Philipp, A. Woll, P. Purohit, J. Weiss, V. Kannan, K. Ramesh, P. Kenesei, J. Okasinski, J. Almer, M. Zhao, A. Ananiadis, T. Hufnagel, Time-resolved x-ray diffraction techniques for bulk polycrystalline materials under dynamic loading, Rev. Sci. Instrum. 85 (2014) 093901.

[26] D. Fan, L. Lu, B. Li, M.L. Qi, J.C. E, F. Zhao, T. Sun, K. Fezzaa, W. Chen, S.N. Luo, Transient x-ray diffraction with simultaneous imaging under high strain-rate loading, Rev. Sci. Instrum. 85, 2014, p. 113902.

[27] M. Hudspeth, B. Claus, S. Dubelman, J. Black, A. Mondal, N. Parab, C. Funnell, F. Hai, M.L. Qi, K. Fezzaa, S.N. Luo, W. Chen, High speed synchrotron x-ray phase contrast imaging of dynamic material response to split Hopkinson bar loading, Rev. Sci. Instrum. 84 (2013) 025102.

[28] T. Sun, K. Fezzaa, HiSPoD: a program for high-speed polychromatic x-ray diffraction experiments and data analysis on polycrystalline sample, J. Synchrotron Radiat. 23, 4.

[29] B.X. Bie, J.Y. Huang, B. Su, L. Lu, D. Fan, J.C. E, T. Sun, K. Fezzaa, M. L. Qi, S. N. Luo, Dynamic tensile deformation and damage of B$_4$C-reinforced Al composites: time-resolved imaging with synchrotron x-rays, Mater. Sci. Eng. A, 664, 2016, pp. 86–93.

[30] J.Y. Huang, J.C. E, J.W. Huang, T. Sun, K. Fezzaa, S.L. Xu, S.N. Luo, Dynamic deformation and fracture of single crystal silicon: fracture modes, damage laws, and anisotropy, Acta Mater. 114, 2016, pp. 136–145.

[31] M.R. Barnett, Z. Keshavarz, A.G. Beer, X. Ma, Non-schmid behaviour during secondary twinning in a polycrystalline magnesium alloy, Acta Mater. 56 (2008) 5–15.

[32] B. Wang, R. Xin, G. Huang, Q. Liu, Strain rate and texture effects on microstructural characteristics of Mg-3Al-1Zn alloy during compression, Scr. Mater. 66 (2012) 239–242.

[33] D. Brown, I. Beyerlein, T. Sisneros, B. Clausen, C. Tomé, Role of twinning and slip during compressive deformation of beryllium as a function of strain rate, Int. J. Plast. 29 (2012) 120–135.

[34] F. Kabirian, A.S. Khan, T. Gnäupel-Herlod, Plastic deformation behavior of a thermo-mechanically processed AZ31 magnesium alloy under a wide range of temperature and strain rate, J. Alloy Compd. 673 (2016) 327–335.

[35] L. Lu, B.X. Bie, Q.H. Li, T. Sun, K. Fezzaa, X.L. Gong, S.N. Luo, Multiscale measurements on temperature-dependent deformation of a textured magnesium alloy with synchrotron x-ray imaging and diffraction, Acta Mater. 132 (2017) 389–394.